# Ambient noise tomography of the East African Rift in Mozambique

Ana Domingues,[1,2,*] Graça Silveira,[3,4] Ana M.G. Ferreira,[5,6] Sung-Joon Chang,[7]
Susana Custódio[3] and João F.B.D. Fonseca[1]

[1] *Laboratório de Sismologia, 6º, Piso do Complexo Interdisciplinar, Instituto Superior Técnico, Av. Rovisco Pais 1, 1049-001 Lisboa, Portugal.*
E-mail: *ana.domingues@ist.utl.pt*
[2] *Department of Earth and Planetary Sciences, Birkbeck, University of London, London WC1E 7HX, United Kingdom*
[3] *Instituto Dom Luiz, Faculdade de Ciências, Universidade de Lisboa, Campo Grande, Ed. C8, Piso 3, Gab. 5 (8.3.05) 1749-016 Lisbon, Portugal*
[4] *Instituto Superior de Engenharia de Lisboa—ISEL, Rua Conselheiro Emídio Navarro, 1, 1959-007 Lisbon, Portugal*
[5] *Department of Earth Sciences, University College London, London WC1E 6BT, United Kingdom*
[6] *CEris, ICIST, Instituto Superior Técnico, Universidade de Lisboa, Lisbon, Portugal*
[7] *Division of Geology and Geophysics, Kangwon National University, Chuncheon, Gangwon-do 24341, South Korea*

## SUMMARY

Seismic ambient noise tomography is applied to central and southern Mozambique, located in the tip of the East African Rift (EAR). The deployment of MOZART seismic network, with a total of 30 broad-band stations continuously recording for 26 months, allowed us to carry out the first tomographic study of the crust under this region, which until now remained largely unexplored at this scale. From cross-correlations extracted from coherent noise we obtained Rayleigh wave group velocity dispersion curves for the period range 5–40 s. These dispersion relations were inverted to produce group velocity maps, and 1-D shear wave velocity profiles at selected points. High group velocities are observed at all periods on the eastern edge of the Kaapvaal and Zimbabwe cratons, in agreement with the findings of previous studies. Further east, a pronounced slow anomaly is observed in central and southern Mozambique, where the rifting between southern Africa and Antarctica created a passive margin in the Mesozoic, and further rifting is currently happening as a result of the southward propagation of the EAR. In this study, we also addressed the question concerning the nature of the crust (continental versus oceanic) in the Mozambique Coastal Plains (MCP), still in debate. Our data do not support previous suggestions that the MCP are floored by oceanic crust since a shallow Moho could not be detected, and we discuss an alternative explanation for its ocean-like magnetic signature. Our velocity maps suggest that the crystalline basement of the Zimbabwe craton may extend further east well into Mozambique underneath the sediment cover, contrary to what is usually assumed, while further south the Kaapval craton passes into slow rifted crust at the Lebombo monocline as expected. The sharp passage from fast crust to slow crust on the northern part of the study area coincides with the seismically active NNE-SSW Urema rift, while further south the Mazenga graben adopts an N-S direction parallel to the eastern limit of the Kaapvaal craton. We conclude that these two extensional structures herald the southward continuation of the EAR, and infer a structural control of the transition between the two types of crust on the ongoing deformation.

**Key words:** Seismic tomography; Continental margins: divergent; Crustal structure.

## 1 INTRODUCTION

The East African Rift (EAR) presents a unique opportunity to study the different stages of rifting from initiation to breakup (Ebinger 2005). In the last three decades, the EAR has been extensively investigated, mostly from the Afar to the Malawi region (Chorowicz

2005). However, central and southern Mozambique, at the southern end of the EAR, lack geological and geophysical studies to illuminate the continuation of the rift south of Malawi (Ebinger *et al.* 1987). The M7 2006 Machaze earthquake in central Mozambique (Fenton & Bommer 2006; Yang & Chen 2008; Raucoules *et al.* 2010) prompted a renewed interest in the active tectonics of the region and its role in the rifting process.

Mozambique is flanked on its eastern side by the Indian Ocean and on its western side by the Kaapvaal (2.7–3.6 Ga) and the Zimbabwe (2.5–3.0 Ga) cratons, which are separated by the

*Also at: CERENA, Instituto Superior Técnico, Universidade de Lisboa, Avenida Rovisco Pais, 1, 1049-001 Lisboa, Portugal.
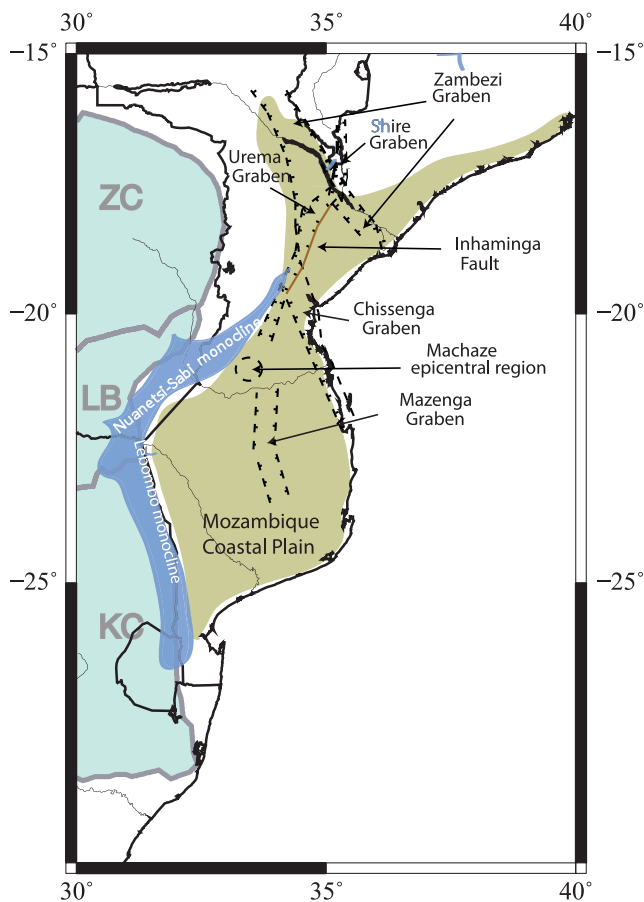
**Figure 1.** Simplified map of Mozambique with the main geological and tectonic units. ZC—Zimbabwe craton; LB—Limpopo; KC—Kaapvaal craton. Adapted from Flores (1973), Nairn *et al.* (1991), Salman & Abdula (1995), Lachelt (2004) and Fonseca *et al.* (2014).

Limpopo belt (2.7 Ga) (see Fig. 1; Fouch *et al.* 2004). Southern and central Mozambique are dominated by a deep upper Cretaceous and Tertiary basin, the Mozambique Coastal Plain (MCP). Fig. 1 sketches the main tectonic provinces. The Kaapvaal Province is composed by granitoids and granites, including deformed greenstone of ultrabasaltic and basic volcanics (Lachelt 2004). The Zimbabwe craton is composed by crystalline basement rocks comprising greenstones, mafic and ultramafic rocks, gneisses and migmatites and late intrusive granites (Carruthers *et al.* 1993). These stable blocks remained almost unaffected by later deformation events such as the Pan-African orogeny (500 Ma) (Kröner & Mainz 2004), the Karoo rifting (Catuneanu *et al.* 2005) and the East African rifting (Chorowicz 2005). It is usually assumed (e.g. Watkeys 2002) that the eastern limit of the cratonic crust coincides with the Lebombo monocline (Kaapval craton) and with the Nuanetsi-Sabi monocline (Zimbabwe craton), but the location of this limit is obscured by the sedimentary cover.

The geology of Mozambique is composed mainly by Precambrian and Cenozoic terrains (Lachelt 2004). The crystalline Precambrian basement, ranging from Archean to Upper Proterozoic, is located mainly in the north and northwest of the country. Mesozoic sedimentary rocks are present in central and northern Mozambique, while Tertiary and Quaternary sediments dominate in the south of the country. In central and southern Mozambique, the sediments of the MCP are underlain at a depth of ∼3200 m by a basaltic basement formed during the Mesozoic or Karoo rifting (Flores 1973). The

Cenozoic deformation is characterized by the formation of grabens such as the Urema and Mazenga graben in Central Mozambique (Hartnady 2006), controlled by active tectonic structures of the Inhaminga and Zambezi tectonic systems (Flores 1973) depicted in Fig. 1.

Some key questions about the structure and geological evolution of this region remain unanswered: Where is the transition from stable cratons to rifted crust in Mozambique? What is the relationship between tectonic units and local seismicity? Which structures in central and south Mozambique are the continuation of the known structures of the EAR further north in the country and across the border in Malawi? The nature of the crust underneath the MCP is another topic still under debate, with previous studies favouring a continental crust (Watkeys 2002), thinned continental or transitional crust (Watts 2001) or oceanic crust type (Leinweber & Jokat 2011). Based on gravity data, Watts (2001) proposed that the crust of the MCP margin might be thinned transitional crust probably of oceanic rather than continental origin. Supported by magnetic and gravity methods, Leinweber & Jokat (2011) suggested that this region is floored by thickened oceanic crust. However, the detailed nature of the crust is still unknown due to the non-existence of geophysical models for the region. In order to clarify the properties of the crust beneath Mozambique, this study analyses ambient seismic noise using a set of 30 broad-band seismic stations temporarily deployed in the region (Fonseca *et al.* 2014). The principle of ambient noise interferometry is based on the idea that the cross-correlation of a diffuse wavefield recorded by two separate instruments is proportional to the empirical Green's function between the two stations. A Green's function is the impulse response of a medium and contains information about wave propagation, hence medium properties, between the two sites. This idea was originally presented by Aki (1957), but it was not applied to seismology until the beginning of the 2000s. This concept was proved in acoustic laboratory experiments (Lobkis & Weaver 2001), as well as theoretically (e.g. Lobkis & Weaver 2001; Wapenaar 2004; Roux *et al.* 2005). Later, Campillo & Paul (2003) and Shapiro & Campillo (2004), applied the concept to seismic data. These studies focus on periods in the 5–100 s band, which contain the so-called microseismic and 'Earth hum' bands. Many studies have used ambient noise tomography (ANT) around the globe to infer crustal and upper-mantle Earth structure, from local to continental scales, yielding high-resolution models (e.g. Sabra *et al.* 2005; Shapiro *et al.* 2005; Ritzwoller *et al.* 2011, for the United States). In this study, we perform seismic ANT using data with wave periods $T \sim$ 5–40 s from 30 stations from MOZART network and complemented by data from two AfricaArray stations (Nyblade *et al.* 2011). We obtain group velocity maps of Mozambique and, in addition, we derived four 1-D models for shear wave velocity versus depth at selected points distributed over the study area, to characterize the crust of the different tectonic provinces.

## 2  DATA

### 2.1  Data acquisition

As part of the MOZART Project (MOZambique African Rift Tomography) (Fonseca *et al.* 2014) a network with 30 three-component seismic broad-band stations, loaned from the SEIS-UK equipment pool, was deployed in central Mozambique. The network was deployed for a total of 26 months. In order to obtain a wide regional coverage, the stations were spread between NE South Africa and
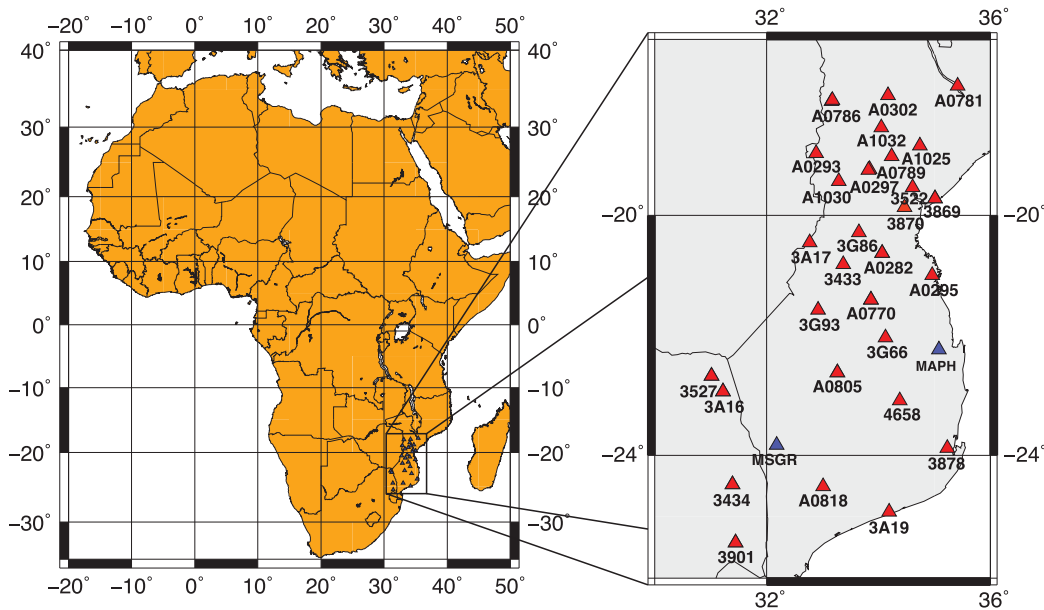
**Figure 2.** Map of the MOZART broad-band seismic network located in Mozambique, in the southeast of Africa. The close-up map of the network (right) shows the location of stations from the MOZART (red triangles) and AfricaArray networks (blue triangles).

central and southern Mozambique (Fig. 2). In addition to using data from the MOZART network, we also used data from two stations of the AfricaArray network located in the study area (Nyblade *et al.* 2011). Interstation distances vary between 35 and 940 km, with an average interstation distance of approximately 100 km.

## 2.2 Seismic waveform processing

We process and carry out group velocity measurements on the vertical component of the available data following a procedure adapted from Bensen *et al.* (2007). The process is divided into three main phases: (1) Single station data preparation; (2) Computation of cross-correlations and stacking between pairs of stations; (3) Group velocity measurements and data selection.

The main goal of Phase 1 is to emphasize the ambient noise present in the data. We remove the instrument's response, as well as the data's mean and trend. A fourth-order bandpass Butterworth filter is applied in the period range $T \sim 2$–55 s and data are divided into time-series of a single day for each station. Subsequently, a spectral domain normalisation is applied (spectral whitening). The main purpose of the spectral whitening is to broaden the ambient noise spectra. It also reduces any monochromatic noise from the data.

In order to minimize the effect of earthquakes on the cross-correlations, we applied a temporal normalisation. We tested two different temporal normalisation methods: the clipping method, used by Sabra (2005) and the RAMN (Running Absolute Mean Normalisation) technique used by Bensen *et al.* (2007). The first temporal normalisation method clips the waveform above the standard deviation of the signal for a given day. The RAMN method computes the running average of the absolute value of the waveform in a normalisation time window of fixed length. We applied both methods to our data and concluded that RAMN is a more reliable method for efficiently eliminating earthquakes (see Supplementary material Fig. S1). We performed spectral whitening before temporal normalisation in order to decrease the loss of long-period signals. Performing temporal normalisation on an un-whitened time-series

normalises mainly the microseismic noise (dominant between 8 and 16 s period) (Cessaro 1994).

## 2.3 Cross-correlation and data selection

In Phase 2, we compute the cross-correlations and employ a three-stage stacking. We calculate cross-correlations of one-hour data segments and perform a stack for each day between all pairs of available stations, thus obtaining a daily cross-correlation per pair of stations. Subsequently, an annual stack is performed for each year (2011, 2012 and 2013) and a final stack of the three years is computed. The significance of using long time-series is illustrated in Fig. S2 in the Supplementary Material. An improvement in the signal-to-noise ratio (SNR) between one day cross-correlation and the six-month stacked correlation is clearly observed.

The cross-correlation computation results in a two-side signal with negative and positive time coordinates, usually called the 'acausal' and 'causal' components, respectively (see Fig. 3). The amplitude of both causal and acausal sides of the cross-correlation contains information about the strength, density and location of the sources of seismic noise recorded by the stations. A homogeneous distribution of similar types of sources around two stations generates symmetric cross-correlations with identical amplitude signals in the negative and positive sides (Yang & Ritzwoller 2008). However, most often the noise sources are not evenly distributed in time and space, and they do not always have the same characteristics, which leads to asymmetric cross-correlations, as illustrated in Fig. 3. We investigated the seasonal variability of the ambient noise recorded by the MOZART network, by stacking three months of daily data during the 2012 Southern Hemisphere summer (December to March) and winter (June to September). The differences observed between the two seasons are minor (Fig. 3), indicating no significant seasonal variability in the data. This observation is in good agreement with the background noise analysis previously done with data of the MOZART network (Fonseca *et al.* 2014), which shows that the median noise amplitudes recorded during the months of summer and winter have similar amplitudes (Fig. 4). The
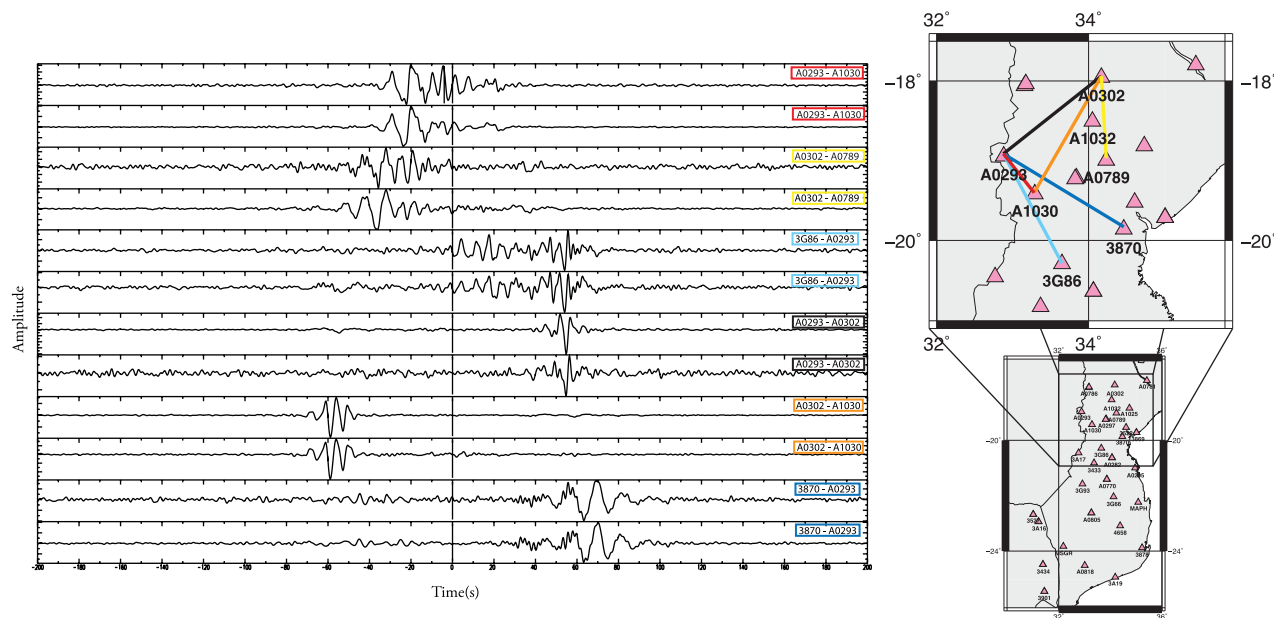
**Figure 3.** Examples of cross-correlations of ambient noise for different orientations of station paths and season. We present two cross-correlations per interstation path; the first is the correlation stack of data available during the South Hemisphere's winter and the second is the correlation stack of data available during the South Hemisphere's summer. The map on the right-hand side of the figure shows the paths presented in the cross-correlation plot. The colour of the paths corresponds to the cross-correlations with the legend highlighted with the same colour.
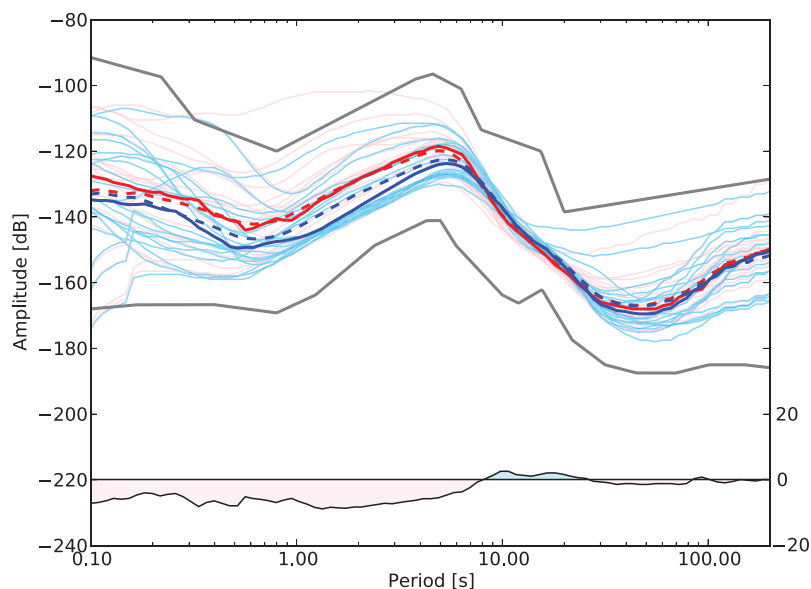


**Figure 4.** Median noise amplitudes of vertical ground motion recorded at all stations during the winter months of June, July and August (light blue lines) and during the summer months of December, January and February (light red lines), based on the computation of power spectral densities (PSDs) of continuous seismic data. The thick and dashed lines, respectively, show the medians and average of all the station noise levels recorded during the months of winter (blue) and summer (red). At the bottom is a black curve that represents the difference between noise recorded during winter and summer months (scale on the right side). The shaded area under this curve is light blue or light red depending on whether the noise is higher in the winter or summer, respectively. The seasonal noise difference is very small for the period band we focused on in this study ($T \sim 5$–40 s), but higher at very short periods.

background noise analysis was based on the methodology proposed by Mcnamara & Buland (2004), implemented in the software package ObsPy (Beyreuther *et al.* 2010), and then adapted as described in Custódio *et al.* (2014).

Higher amplitude arrivals coming predominantly from one side of the network can be observed in Fig. 3 (e.g. station pairs 3G86-A0293), leading to asymmetric cross-correlations. The noise sources seem to be located mainly northeast (pairs A0293-A0302 and A0302-A1030), south (pair A0302-A0789) and southeast (pairs

A0293-A1030, 3G86-A0293 and 3870-A0293) of the network, which is likely related to seismic noise generated in the nearby Indian Ocean. In order to obtain symmetric cross-correlations, we averaged the causal and acausal components, which results in the so-called symmetric component (Lin *et al.* 2006). From this stage on we used just one side of the signal, which now contains all information.

Fig. 5 shows examples of cross-correlations obtained for different station pairs, from south to central Mozambique.
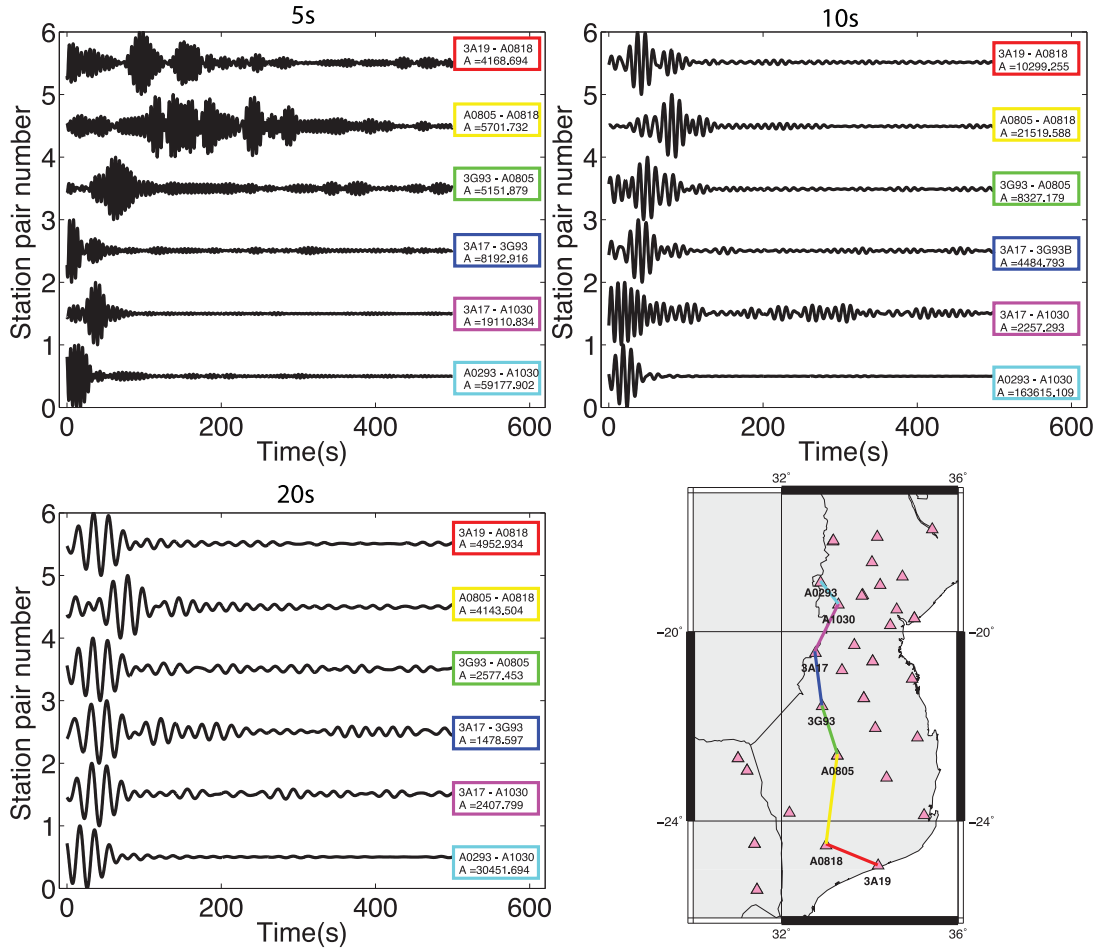
**Figure 5.** Behaviour of the empirical Green's functions for various station pairs filtered for dominant wave periods of $T \sim 5$, 10 and 20 s. The effects of sedimentary basins are clearly observed in the $T \sim 5$ s waveforms. The colour of the paths in the bottom right map corresponds to the cross-correlation with the legend highlighted with the same colour in each plot. All the cross-correlations are self-normalised to 1 and the corresponding maximum amplitudes are shown in the coloured box. Empirical Green's functions are plotted according to station locations, from south to north.

Examples of data filtered with various different dominant periods are shown. For station pairs 3A19-A0818, A0805-A0818 and 3G93-A0805, the cross-correlations filtered around $T \sim 5$ s show several reverberations which are not displayed if the filtering is applied around $T \sim 10$ or 20 s. These complex signals are located mainly in southern Mozambique, in particular in the MCP (Fig. 1). In order to better understand this observation, we tested several other network paths. A similar behaviour is observed for paths within this region, which confirms that these signals are due to the sedimentary basins in the region. For longer wave periods, sensitive to deeper structure, cross-correlations show simpler waveforms.

## 2.4 Signal-to-noise ratio analysis

To estimate the quality of the empirical Green's functions, we performed an SNR analysis. The SNR study is key to obtain reliable dispersion measurements, as it will lead to the exclusion of poor-quality cross-correlations. We computed cross-correlation time-series with a length of 1500 s and filtered them around different dominant periods. The purpose of such long time-series was to ensure that it was possible to select two separate windows: one only with signal and

another only with noise, respectively. The SNR was calculated as follows:

$$\mathrm{SNR} = \sqrt{\frac{\displaystyle\sum_{i=N1,N2} s_i^2}{\displaystyle\sum_{j=N1+1000,N2+1000} n_j^2}}, \tag{1}$$

where $s$ and $n$ are discrete time-series of the signal and noise selections, respectively. The signal window selection (starting at time $N1$ and ending at time $N2$) was based on a velocity range containing the IASP91 (Kennett & Engdah 1991) group velocities for each period. By starting the noise window 1000 s after the end of the signal window allowed a clear separation of the two.

Fig. 6 shows the SNR as a function of interstation distance (Fig. 6a) and of azimuth (Fig. 6b) for $T \sim 5$ s. As expected, the SNR decreases with increasing distance between pairs of stations. The same trend was observed for other wave periods. Cross-correlations from more distant station pairs tend to be noisier due to the loss of coherent surface wave energy in the noise wavefield between the two stations. The variation of the SNR with station pair azimuth was also investigated. Although we do not observe a strong variation of the SNR with azimuth (Fig. 6b), we find that the SNR values are lower for north–south orientation paths, which are typically the
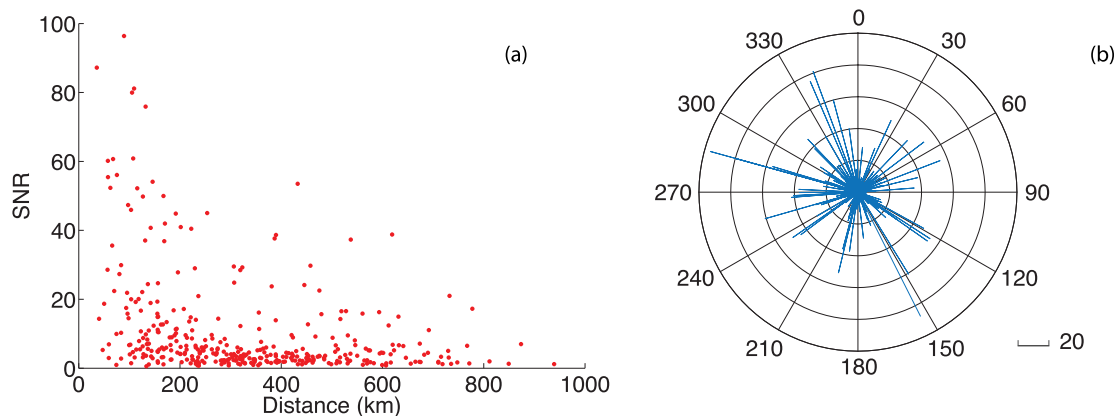
**Figure 6.** SNR values as a function of (a) distance and (b) of azimuth between all pairs of stations ($T \sim 5$ s).

**Table 1.** Total number of initial measurements, number of measurements discarded by SNR analysis, by frequency–time analysis and total number of remaining measurements used for group velocity tomography.

| | |
|---|---|
| Total waveforms | 378 |
| Waveforms rejected by SNR (SNR < 7) | 65 |
| FTAN measurement rejections | 36 |
| Total remaining measurements | 277 |



**Figure 7.** Rayleigh wave group velocity dispersion curves retrieved using a frequency–time analysis. Each coloured group velocity curve represents a station pair measurement. A synthetic group speed dispersion curve from IASP91 model (Kennett & Engdah 1991) (red thick dashed line) is shown for reference.

longest paths. This decrease in SNR is probably due to contamination by non-coherent noise signals and orientation (perpendicular to preferred ambient noise propagation).

Based on the SNR analysis, we selected the highest quality cross-correlations. Measurements with SNR > 7 correspond to clear empirical Green's functions. Thus, we classified as good quality cross-correlation those with SNR > 7 and eliminated those with SNR < 7 (see Table 1 and Supplementary Fig. S3).

## 3 GROUP VELOCITY MEASUREMENTS

After the SNR analysis, we focused on measuring the group velocity dispersion curves. As explained in Section 2.3, we only use vertical component data, and therefore we only obtain dispersion measurements for Rayleigh waves.

The measurements were performed applying a multiple filter technique, the Frequency–Time ANalysis (FTAN; Herrmann & Ammon 2004). It consists of filtering the trace with several narrow bandpass Gaussian filters with different centre frequencies. An inverse Fourier transform is then applied to each bandpass function resulting in a 2-D envelope frequency–time function. Knowing the centre frequency of the Gaussian filters ($w_0$) associated with the envelope and the distance between the pair of stations ($r$), the group velocity $U(w_0)$ is determined by measuring the maximum of the envelope function: $U(w_0) = r/\tau(w_0)$, where $\tau(w_0)$ is the group arrival time (Bensen *et al.* 2007). By converting the different centre frequencies to wave periods, it is possible to construct a period-group velocity diagram, that is, a dispersion curve. In Fig. 7, we present all dispersion curves obtained for different pairs of stations, where the group velocity is shown to increase with increasing period. We measured group velocities of Rayleigh waves from $T \sim 3$ to 50 s. The black thick dashed line is a group velocity curve computed from the global model IASP91 (Kennett & Engdah 1991), for comparison with our measurements. Dispersion curves were rejected if they displayed artificial jumps or abrupt changes and/or if it was not possible to obtain the absolute maximum of the envelope function.
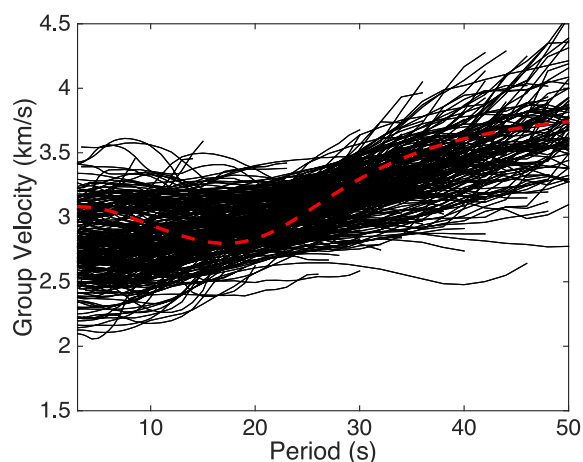
Approximately one-fourth of the cross-correlations were rejected due to low SNR and FTAN measurement failure (Table 1).

In order to obtain an estimation of the FTAN measurement error and stability, we performed the error analysis illustrated in Fig. 8. We chose three different cross-correlations with the following properties: (i) station paths crossing very different regions; and, (ii) different number of daily cross-correlations used to compute the stack. 3A16-3G86 is the pair whose stack was based on a higher number of daily cross-correlations with more daily cross-correlations (262 d). Station pair 3A17-4658 comprises 97 d of cross-correlations, while pair 3870-3G66 is based on only 38 d of cross-correlations. We started by randomly calculating 10 different stacks with one-third of the available cross-correlations. For instance, for pair 3A16-3G86, with 262 daily cross-correlations available, we randomly selected 87 cross-correlations for each of the 10 stacks performed. Group velocities were measured for the 10 cross-correlation and stacked. The resulting dispersion curves are presented for the three different station pairs in Figs 8(a), (c) and (e). Dispersion measurements tend to be more divergent, and therefore present higher uncertainties, at longer periods. Yet they remain similar to the original measurement performed using all cross-correlations available. Also, we observe in Figs 8(c) and (e) some variability of short-period measurements ($T \sim 3$–8 s) that may be related with the waveform complexities
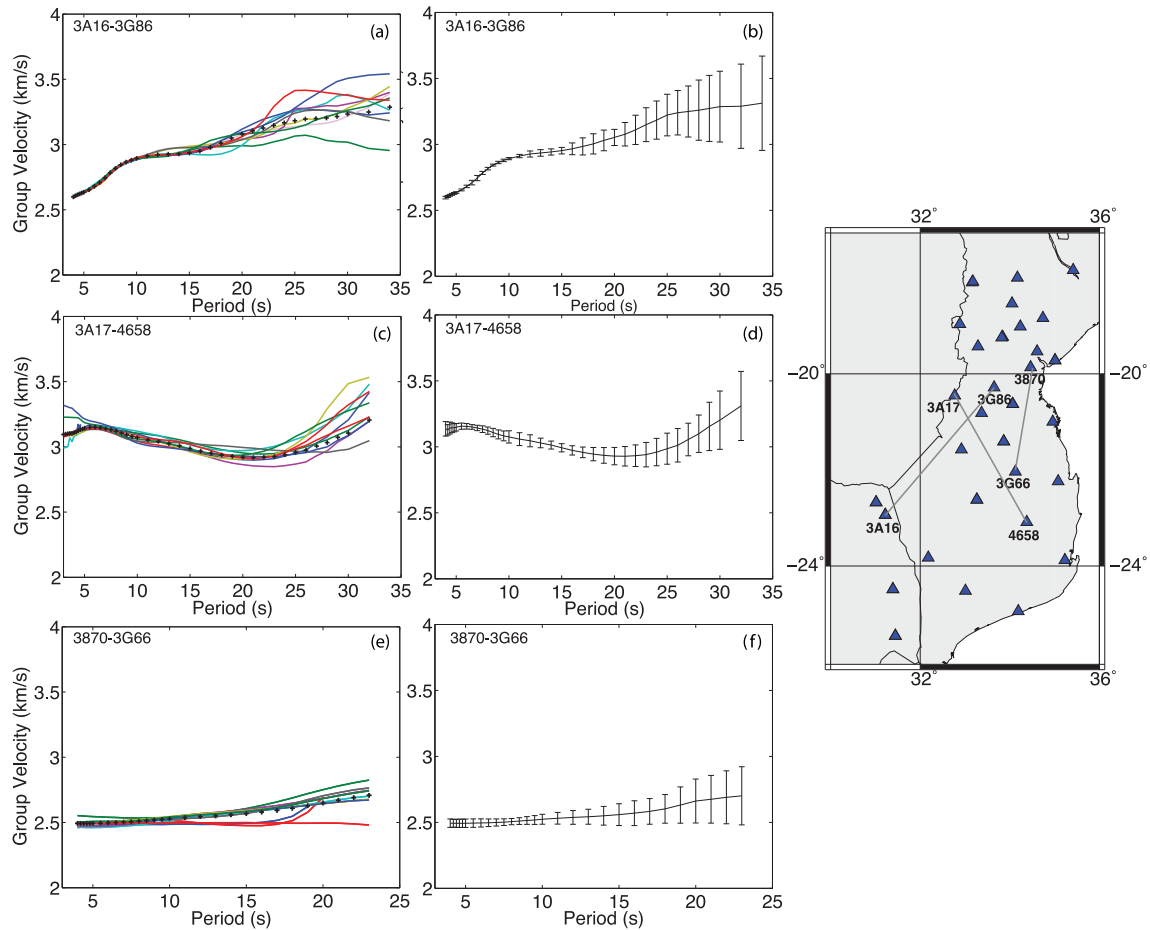
**Figure 8.** Error estimation of the group velocity measurements for three different dispersion curves. Graphs (a), (c) and (e) show 10 different measurements represented in different colours for a given pair of stations (see the text for more details). The dispersion curve based on all available cross-correlation is plotted in black crosses. Station paths are indicated in grey lines in the map on the right. Graphs (b), (d) and (f) show the average of the 10 different measurements with the associated standard deviation bars.

previously mentioned for the 5 s filtered cross-correlations (see Section 2.2 and Fig. 5). Figs 8(b), (d) and (f) show this variability through wider uncertainties at the beginning and end of the dispersion curves.

# 4 GROUP VELOCITY MAPS

In order to obtain group velocity maps, we used the Fast Marching Surface Tomography (FMST) method (Rawlinson *et al.* 2008), a non-linear tomographic inversion scheme. The FMST combines the Fast Marching Method (FMM) for the forward computation with a subspace method (Kennett *et al.* 1988) for inversion. In order to account for the non-linearity of the inverse problem, the two steps are applied iteratively. We performed a total of six iterations. The FMM is a grid-based numerical algorithm that solves the eikonal equation, which describes the propagation of seismic waves in the high-frequency limit, by a finite-difference scheme (Rawlinson & Sambridge 2005). The subspace method, a hybrid between steepest descent and matrix methods, solves the inverse problem of adjusting the model parameters to satisfy the observed data and the regularisation constraints. Smoothing and damping regularisation provides additional constraints on the model parameters, helping stabilise the inversions. The damping and smoothing factors chosen were $\epsilon = 0.5$ and $\eta = 2$, respectively, based on several tests with different regularisation combinations. The models were defined by a

grid of nodes with bicubic B-spline interpolation. The dimensions of the grid are 0.52° N–S by 0.34° E–W and were chosen based on synthetic checkerboard tests with different grid space sizes.

We performed synthetic checkerboard resolution tests based on the available path distribution. Gaussian noise was added to the synthetic data with a standard deviation of 0.15 s. Gaussian noise is needed in order to simulate the noise content of the observed traveltimes. In Fig. 9 we present the input synthetic checkerboards for $T \sim 5$, 20 and 30 s, as well as the recovered anomalies. For improved visibility, the paths used for each checkerboard are not plotted in Fig. 9. Nevertheless, it is important to bear in mind that the number of paths used decreases with increasing period. We discarded measurements for interstation distances shorter than three wavelengths, beyond which a degradation of the dispersion measurements is observed (Bensen *et al.* 2007). We observe that as the period increases, the resolution decreases, as a consequence of this 'wavelength rule'. There are also some differences in the recovery patterns observed for the northern and southern sections of the study region. For instance, Fig. 9(d) shows that in the southwest region the anomalies are smeared and become elongated in the NE-SW direction, indicating that path coverage is not very good. This effect is not observed in the northern region, where there is a large number of uniformly distributed stations. In the northern region, the resolution slightly deteriorates at longer periods, in result of the limited interstation distances in this region.
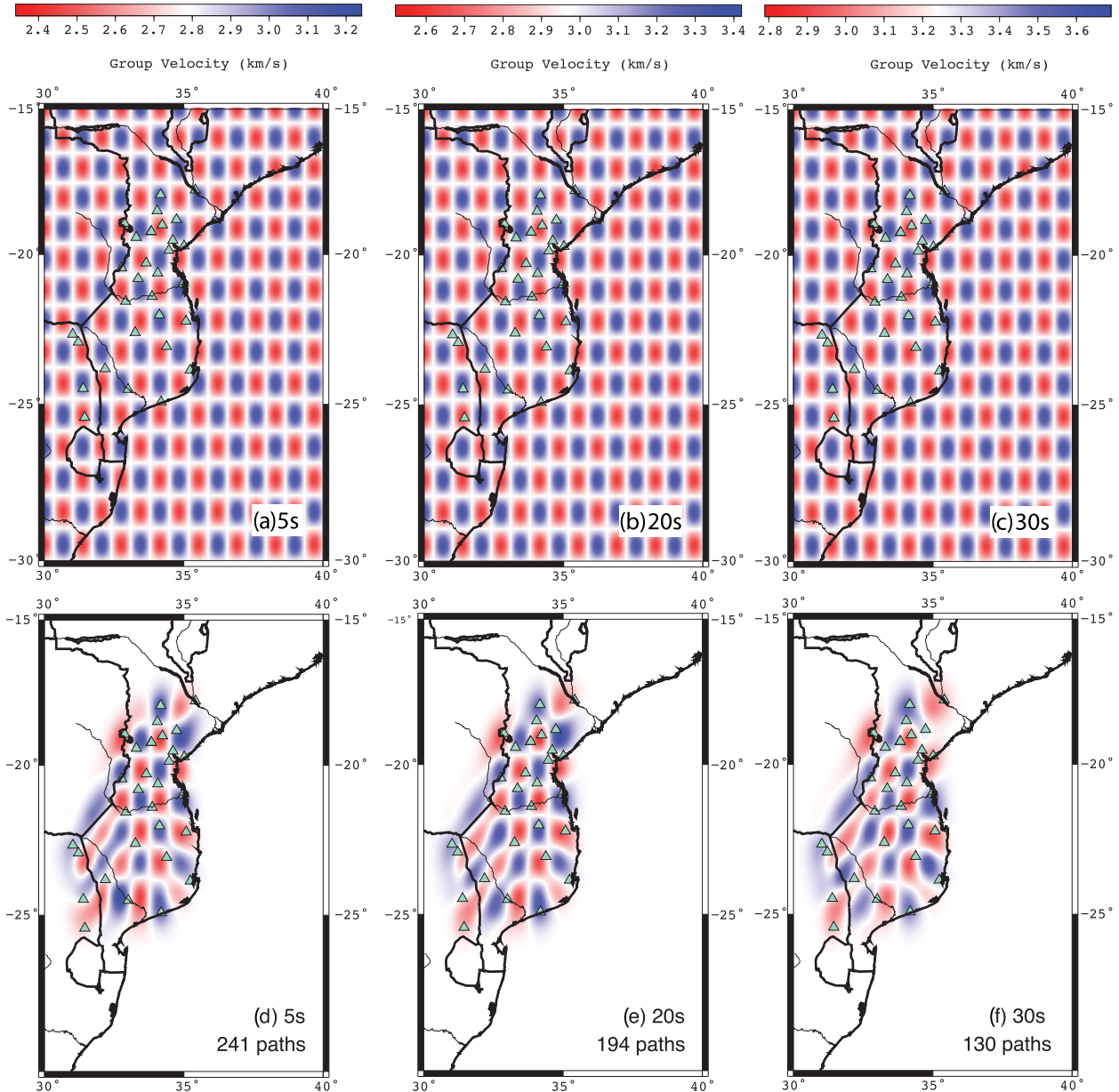
**Figure 9.** Checkerboard tests for wave periods of $T \sim 5$, 20 and 30 s. The maps (a)–(c) on the top represent the input anomalies. These synthetic models are built using checkerboard cells with 0.52° N–S by 0.34° E–W. Maps (d)–(f) on the bottom are the recovered anomalies from the inversion, for the path distribution used in the real data inversions. In the bottom right are indicated the period and number of ray paths used for each inversion.

Finally, we applied the inversion scheme to our real data set and obtained group velocity maps for wave periods between $T \sim 5$ and 36 s (see Fig. 10). We did not use longer period data because we only had few measurements available, resulting in limited resolution. For the starting model we used a constant velocity field calculated from the average velocity of all dispersion measurements for each working period.

The misfits between the observed and the synthetic dispersion measurements are presented in Table 2. The root mean square (rms) is given by:

$$\text{rms} = \sqrt{\frac{\sum_{i=0}^{nt}(tm_i - to_i)^2}{nt}}, \tag{2}$$

where $nt$ corresponds to the number of traveltimes available for each period, $tm$ is the model traveltime and $to$ is the observed

traveltime. The standard deviation (std) is given by: std $= \sum_{i=0}^{nt}(tm_i - to_i)^2/(nt - 1)$. rms and std values are calculated at each iteration based on a starting model (rms$_{initial}$, iteration 0) and the final model calculated (rms$_{final}$, iteration 6). std$_{initial}$ and std$_{final}$ are the data standard deviation of the starting and final models, respectively. We observe that, for the $T \sim 5$ s inversion, there is an improvement in data fit of approximately 30 per cent with respect to the starting model. Although the number of paths used at this period is significant, overall, the paths in the MCP are reduced, as explained above in Section 2.3. The $T \sim 15$ and 20 s inversions show a substantial improvement in the data fit of more than 50 per cent with respect to the starting model, and the inversion for periods of $T \sim 10$ and 30 s show a data fit amelioration of 40 per cent. These inversions ($T \sim 10$–30 s) were performed using a high number of group velocity measurements, leading to the most substantial
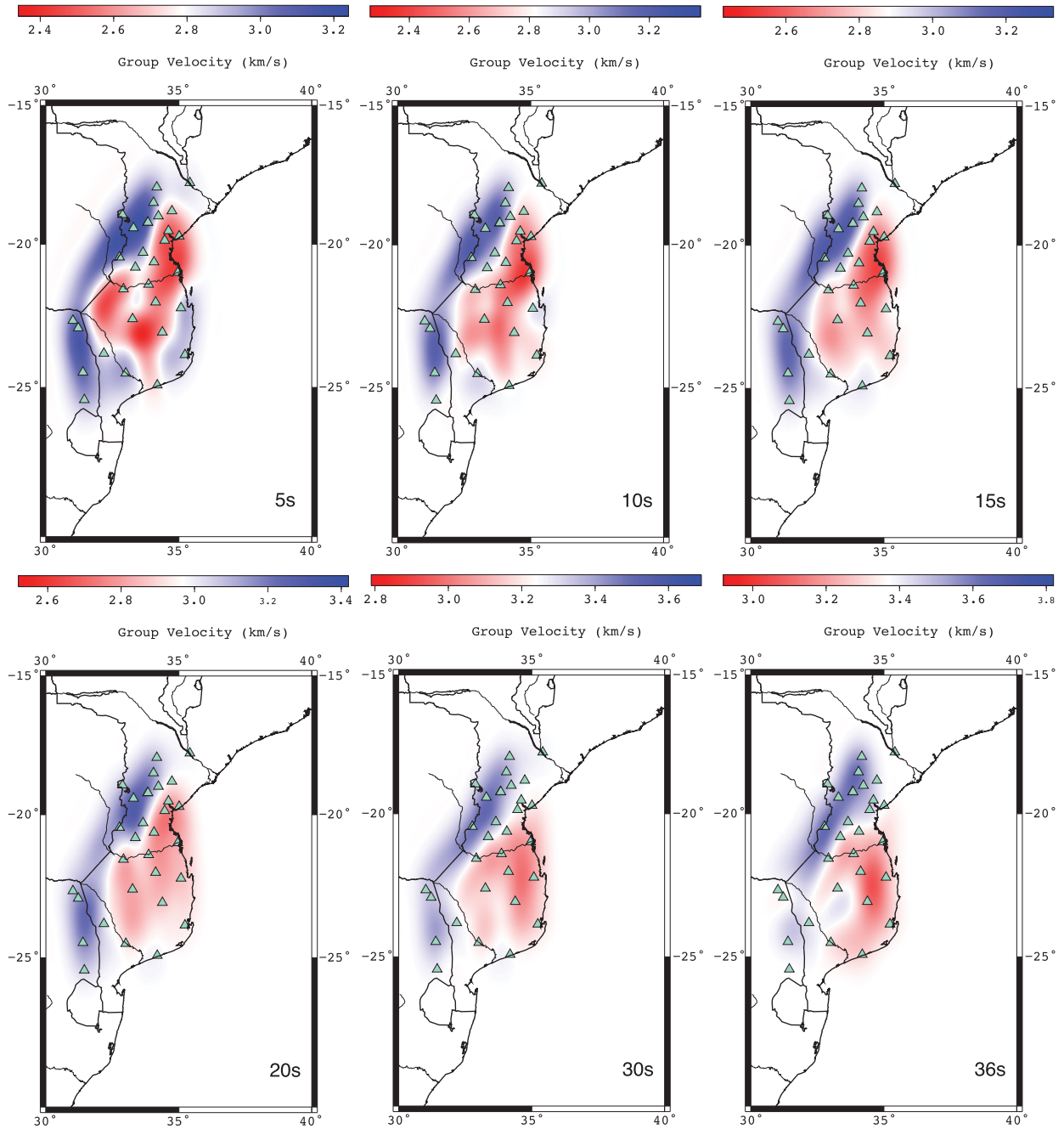
**Figure 10.** Rayleigh wave group velocity maps for Central Mozambique obtained from ambient noise data. Group velocity map for the period of (a) 5; (b) 10; (c) 15; (d) 20; (e) 30 and (f) 36 s.

**Table 2.** Traveltime misfit values for the starting and final models of the group velocity map inversion. The root mean square (rms) is calculated using eq. (2) (see the main text for details).

| Wave period $T$ (s) | $rms_{initial}$ (s) | $rms_{final}$ (s) | $std_{initial}$ (s) | $std_{final}$ (s) |
|---|---|---|---|---|
| 5 | 9.35 | 6.49 | 9.37 | 6.51 |
| 10 | 9.24 | 5.56 | 9.26 | 5.57 |
| 15 | 7.19 | 3.31 | 7.21 | 3.31 |
| 20 | 5.75 | 2.43 | 5.76 | 2.44 |
| 30 | 6.29 | 3.99 | 6.31 | 4.00 |
| 36 | 7.58 | 5.57 | 7.62 | 5.60 |

improvement with respect to the starting model. On the other hand, the enhancement in data fit for the $T \sim 36$ s inversion was lower (27 per cent) mainly due to the reduced number of paths available.

In order to better understand the sensitivity of the group velocity for the different periods used, we calculated the sensitivity kernels for the Kaapvaal and the MCP region (see Supplementary Fig. S4). We observe that different wave periods are sensitive to different depths, with longer periods sampling deeper structures. Therefore, we can identify the general features of the upper crust by looking at short-period ($T \sim 5$ and 10 s) group velocity maps and of the deeper crust by looking at longer period maps ($T \sim 20$ and 25 s). We additionally observe in Fig. 10 that the average group velocities increase as we go to longer periods, indicating that, as expected, surface waves travel faster at greater depths.

The most pronounced characteristics observed at all wave periods are a low velocity zone on the southwest, extending from Central Mozambique to the MCP and a band of high group velocities, extending from Eastern Zimbabwe and Western of Mozambique to Northeastern South Africa. Fig. 10 presents maps with absolute values of group velocities, which allows for the comparison between maps for all measured periods.

## 5 ILLUSTRATIVE 1-D DEPTH INVERSIONS

We performed 1-D *Vs* depth inversions for four different regions of the network. The locations of the models were chosen to characterize two zones of the MCP with contrasting group velocity values (points 1 and 2 in Fig. 11), the Kaapvaal craton (point 3) and the Zimbabwe craton (point 4) (Fig. 11). For the inversion, we extracted group velocity dispersion curves for each point using all the periods available from the group velocity maps. In order to perform the 1-D inversions, we use a linearised inversion scheme from Herrmann (2013) and obtain shear velocity values as function of depth. The scheme applies a damped least-squares algorithm using a 5-km-layer parametrisation (Russell 1987; Julià *et al.* 2000; Herrmann & Ammon 2004). At each iteration the algorithm varies the seismic velocity model until an optimal data fit is achieved. In the absence of a velocity model for the region we used as starting model the crustal structure from the global crustal model CRUST1.0 (Laske *et al.* 2013) and the mantle structure from the global mantle model LLNL-G3Dv3 (Simmons *et al.* 2012) for each chosen region. In order to avoid biasing the Moho depth of the final model, weights were introduced in the two layers adjacent to the Moho that allow changes of the velocity across the boundaries. The best-fitting results are presented in Fig. 11. We performed a total of 40 iterations per inversion, which allowed us to achieve a good data fit. Beyond 40 iterations both the data fit and models obtained did not vary significantly. The inversions for structure beneath points 1 and 3 present a variance reduction of ∼85 per cent and points 2 and 4 of ∼90 per cent. Due to the very low velocities of the starting model in point 2, we opted to divide de first layer in three (the first layer with 1 km thickness and 2 layers with 2 km thickness). We observe that beneath the craton regions the retrieved profiles are not very different from the starting model from CRUST1.0, with slightly higher velocities from about 10 km depth. The thickness of the crust does not seem to vary significantly between points 3 and 4, with the Moho in these models being located around 40 km. In the case of points 1 and 2, we observe a gradual variation of the shear velocities along the profiles turning its interpretation more difficult.

Overall, the results from the inversions suggest a thinning of the crust from point 2 to 1.

## 6 DISCUSSION

By using ambient noise analysis we obtained unique images of the crust and uppermost mantle of Central Mozambique. As expected, group velocity maps display a number of features that are correlated with the geological structures of the region (see Fig. 1). Two main anomalies are common to all group velocity maps, with minor variations: Fig. 10 shows (i) a high velocity anomaly in the western side of the network; and, (ii) a low group velocity anomaly in southeast Mozambique. The maps for periods of 5 and 10 s (Figs 10(a) and (b)), being sensitive only to the upper crust, show a good correlation with the geology of Mozambique. We observe in both maps a high velocity zone corresponding to the Kaapvaal and Zimbabwe cratons, identified in Fig. 1. Sedimentary basins have typically low group velocity values, which is the case of the slow anomaly located in the MCP, a sedimentary basin as explained in Section 1.

In the $T \sim 5$ s map, a high velocity anomaly is observed on the right side of the MCP. This anomaly may not be robust due to poor path coverage. Moreover, we do not observe any clear surface geology features that may explain these anomalies. Path coverage decreases as wave period increases. High velocities beneath the cratons can be seen from short ($T \sim 5$ s) to long periods ($T \sim 36$ s) and agree well with geological knowledge, given that cratons in this region are stable granitic structures with an average crustal thickness of about 40 km (James *et al.* 2003). The same is not true for the slow anomalies. The low velocities that we observe in the short-period maps are in part due to sedimentary basins. However, at longer periods slow anomalies cannot be explained only by the surface geology of the MCP and rather reflect deeper crust (see Supplementary Fig. S4).

As explained before, very few studies have tried to address the crustal nature of the MCP, which is still under debate, notably whether it is of continental or oceanic origin (Watts 2001; Leinweber & Jokat 2011). In order to investigate this issue, we performed the following tests. We compared our ambient noise group velocity curves from the MCP with three theoretical dispersion curves for: (i) the crustal model in IASP91 (Kennett & Engdahl 1991); (ii) a typical oceanic crust (A0 in CRUST2.0) without a water layer and sediments (Bassin *et al.* 2000); and (iii) the CRUST2.0 model in Mozambique (see Fig. 12). From the comparison of these curves we found that overall the ambient noise velocity model in our study region show much slower velocities at short periods than typical continental crust-type theoretical curves. However, the measured curves also have different shapes from the standard curves for oceanic crust, which present distinct dispersion characteristics for this period range. At long periods, we found that our ambient noise curves are more similar to continental crust curves (IASP91 and CRUST2.0 for Mozambique). Theoretical group velocities for oceanic crust are much higher than our measurements. In Fig. 12, we also compared the dispersion curves from the MCP with previous ambient noise studies in the Kaapvaal craton (Kgaswane *et al.* 2009, 2012). We observe that they differ in shape and velocity excluding a continental like crust idea. When comparing with the dispersion curves obtained from ambient noise of paths along the Main Ethiopian Rift (MER) we observe some similarity although the values of the group velocities are in general lower in the MCP than in the MER. We underline that path coverage in the MCP region is poor for long periods and at these periods the mea-
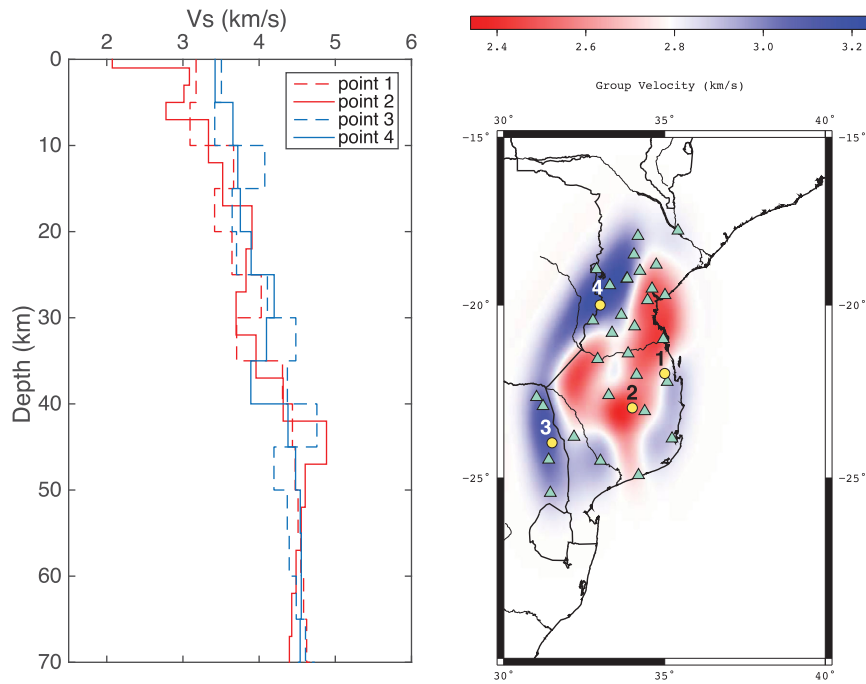
**Figure 11.** 1-D depth inversions profiles for four different selected regions in Mozambique represented with red dots in the map on the right. The lines in red represent the models from the MCP and the blue models represent the cratonic regions of Kaapvaal and Zimbabwe.
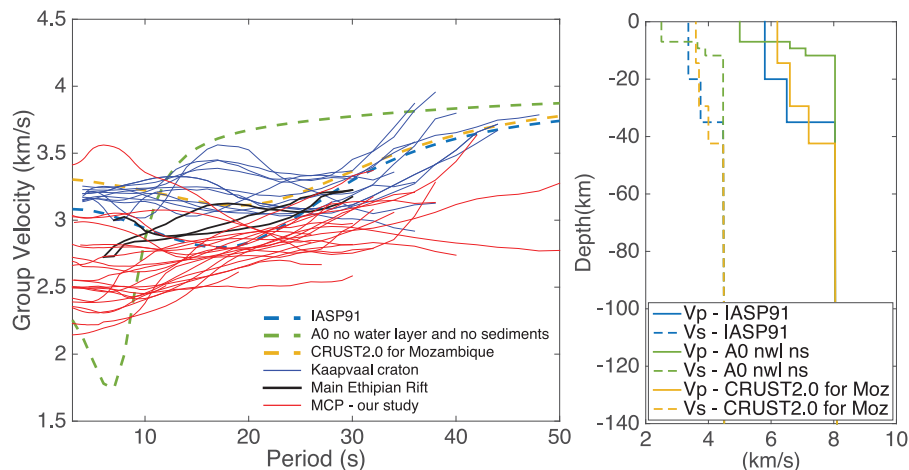


**Figure 12.** Comparison between the ambient noise Rayleigh wave group velocity curves in the MCP (solid red lines) with theoretical group velocity curves for different Earth models (left): IASP91 (Kennett & Engdah 1991) (blue dashed line), A0 from CRUST2.0 without water layer and sediments (green dashed line) and CRUST2.0 for the region of Mozambique (Bassin *et al.* 2000) (yellow dashed line). IASP91 was also used as mantle model to calculate all the theoretical group velocity curves. We compare as well rift like dispersion curves from the Main Ethiopian Rift (Kim *et al.* 2012) (solid black lines) and typical dispersion curves from the Kaapvaal craton (solid blue lines) (Kgaswane *et al.* 2009, 2012). On the right is the correspondent 1-D profile for *S* and *P* velocities of the theoretical models, where A0 nwl ns stands for A0 from CRUST2.0 with no water layer and no sediments.

surements present higher uncertainties (as shown in Fig. 8). The sediments underlying the stations in this region were also a big obstacle in obtaining clear cross-correlations, which may have affected the measurements (Figs 5 and 8). Although the shorter wave period data show some sensitivity to the very shallow structure, there are some uncertainties in the measurements as previously shown. The results of the inversions in the most superficial layer have to be analysed with care, however these values are difficult to reconcile with oceanic crust. The two deep wells drilled in this region—one about 75 km to the north of point 1 and the other nearly coincident with point 2—reached a basaltic basement of Karoo age at depths of 3291 and 3007 m, respectively. Flores (1973), based on magnetic

data, proposed that these basalts were not deposited as a continuous sheet, but as a series of flows through a set of parallel fractures, with ages decreasing from west to east. This emplacement mechanism may have led to a magnetic signature that suggested an oceanic crustal nature, not supported by the seismic velocity profiles or dispersion curve results. The two velocity profiles for the MCP show a slow crust between 20 and 30 km, with velocities below those of the cratonic counterparts, not supporting therefore the presence of a shallow Moho under the MCP. These low crustal velocities along with a thinning of the crust from point 2 to 1 seems to indicate a possible transitional crust from continental to oceanic. Fig. 13 shows that this transition in central and southern Mozambique is
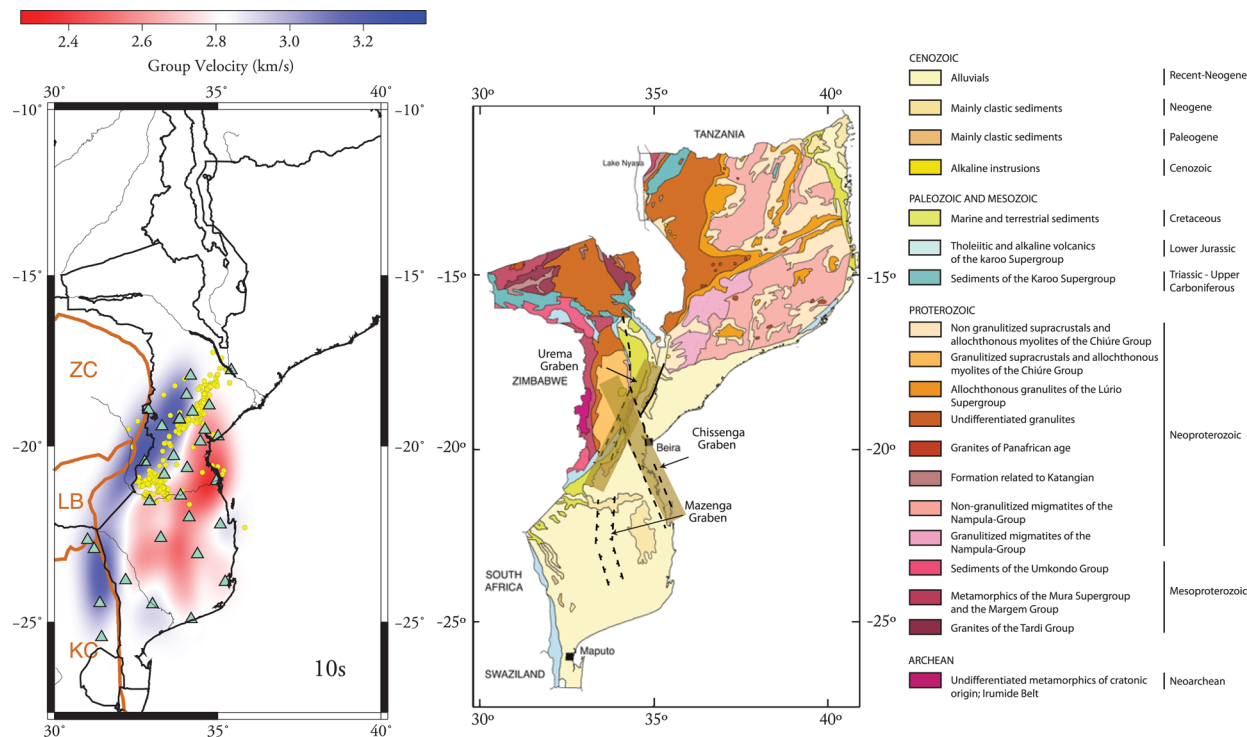
**Figure 13.** Comparison between the Rayleigh wave group velocity map for the period of 10 s (left) with the geological map of Mozambique (modified after Schlüter [2006]) (right). The Zimbabwe craton (ZC) and Kaapvaal craton (KC) are represented with a brown full line as well as the Limpopo Belt (LB). On the left diagram, the seismic stations used are represented by light blue triangles and the local seismicity recorded from the MOZART network until 2012 August (Fonseca et al. [2014]) is shown by yellow circles.

obscured by the sediment cover. Fig. 10 shows a clear NNE-SSW boundary in the northern part of the study area, consistently separating fast from slow crust at all periods. This may indicate that the crystalline basement of the Zimbabwe craton extends further to the east underneath the sediment cover than usually assumed. Further south, the transition between fast and slow crust shifts to the west and runs along the Lebombo monocline, as expected.

The rifting process discussed in the previous two points occurred in the Mesozoic, and led to the opening of the Indian Ocean between southern Africa and Antarctica. It should not be confused with the southward propagation of the EAR, which is responsible for the current seismicity of Mozambique. Fig. 13 shows that the Cenozoic Urema graben (Flores [1973]), which concentrates most of the seismicity recorded (represented by yellow circles) during the MOZART project (Fonseca et al. [2014]), runs along the transition from fast to slow crust. At the southern tip of the region with seismic activity we observe a cluster of events, which marks the location of the 2006 M7 Machaze earthquake and its aftershocks. This earthquake had a normal fault mechanism (Fenton & Bommer [2006]; Raucoules et al. [2010]). It is likely that the ongoing deformation will exploit pre-existing zones of weakness in the lithosphere (Sykes [1978]). The Urema graben connects the rift structures of Malawi (Ebinger et al. [1987]) to the epicentral region of the Machaze earthquake, and is therefore the best candidate for the southward continuation of the EAR. Close to the Machaze epicentre, as can be seen in Fig. 13, the NNE-SSW trend of the Urema graben changes abruptly to N-S along the Mazenga graben (Hartnady [2006]), mimicking the change in direction that can be seen in the eastern limit of the interpreted cratonic crust. The borders of the Mazenga graben may be reactivated Karoo fractures of the type proposed by Flores [(1973])].

While the Mazenga graben does not display significant seismicity in the present, its vicinity to the Machaze epicentre suggests that it is linked to the southward propagation of the EAR. Taking the vertical profile of shear wave velocity for points 1 and 2 (Fig. 11) we observe that the middle crust structure presents slow shear velocities, when compared with points 3 and 4. In the case of the point 2 as representative of the crustal structure of the Mazenga graben, the shallow layers are characterized by slow shear wave velocities, the likely result of poorly consolidated sediments deposited in the very recent geological past. This pulse of extension, not recorded further NE in point 1, may correspond to the first signs of inception of the EAR at this latitude.

## 7 CONCLUSIONS

We applied the ANT technique to data recorded by the MOZART network (30 broad-band stations). We calculated cross-correlations between all the pairs of stations and compute Rayleigh wave group velocity dispersion curves. We obtained Rayleigh wave group velocity maps from ambient noise data in the period range $T \sim 5$–36 s and inverted for 1-D shear wave velocity profiles at four selected locations. The group velocity maps display fast crust towards the west, consistently over all the periods, in agreement with previous studies of the Kaapvaal and Zimbabwe cratons. Toward the east, in the MCP, all the maps show a broad zone of slow crust. A sharp transition between the two types of crust runs through the study area, with an NNE-SSW trend in the northern part and with an N-S trend toward the south. Identifying this transition with the eastern limit of the cratonic crust, we conclude that the Zimbabwe craton seems to extend further east underneath the sediment cover than

usually assumed. The depth inversions suggest that while the craton regions show a typical Moho depth for such structures, in the MCP we observe low crustal velocities along with a thinning of the crust from point 2 to 1 that we interpret as a possible transitional crust from continental to oceanic. Low shear wave velocities in the uppermost levels of the Mazenga graben suggest recent sedimentation, supporting the idea that this structure is the southernmost member of the EAR system. The results suggest that the current location of extensional deformation (Urema rift, Mazenga graben) is controlled by the inherited Mesozoic structures, given the strong correlation with seismicity and the sharp transition between different types of crust revealed by our results.

## ACKNOWLEDGEMENTS

## REFERENCES

Aki, K., 1957. Space and time spectra of stationary stochastic waves, with special reference to microtremors, *Bull. Earthq. Res. Inst.,* **35,** 415–456.

Bassin, C., Laske, G. & Masters, G., 2000. The current limits of resolution for surface wave tomography in North America, *EOS, Trans. Am. geophys. Un.,* **81,** F897.

Bensen, G.D., Ritzwoller, M.H., Barmin, M.P., Levshin, A.L., Lin, F., Moschetti, M.P., Shapiro, N.M. & Yang, Y., 2007. Processing seismic ambient noise data to obtain reliable broad-band surface wave dispersion measurements, *Geophys. J. Int.,* **169**(3), 1239–1260.

Beyreuther, M., Barsch, R., Krischer, L., Megies, T., Behr, Y. & Wassermann, J., 2010. ObsPy: a python toolbox for seismology, *Seism. Res. Lett.,* **81**(3), 530–533.

Campillo, M. & Paul, A., 2003. Long-range correlations in the diffuse seismic coda, *Science,* **299**(5606), 547–549.

Carruthers, R., Greenbaum, D., Jackson, P., Mtetwa, S., Peart, R. & Shedlock, S., 1993. Geological and geophysical characterisation of lineaments in southeast zimbabwe and implications for groundwater exploration, *Tech. rep.,* British Geol. Surv., Nottingham, UK. This item has been internally reviewed but not externally peer-reviewed.

Catuneanu, O., Wopfner, H., Eriksson, P.G., Cairncross, B., Rubidge, B.S., Smith, R.M.H. & Hancox, P.J., 2005. The Karoo basins of south-central Africa, *J. Afr. Earth Sci.,* **43**(1–3), 211–253.

Cessaro, R.K., 1994. Sources of primary and secondary microseisms, *Bull. seism. Soc. Am.,* **84**(1), 142–148.

Chorowicz, J., 2005. The East African rift system, *J. Afr. Earth Sci.,* **43**(1–3), 379–410.

Custódio, S. *et al.*, 2014. Ambient noise recorded by a dense broadband seismic deployment in Western Iberia, *Bull. seism. Soc. Am.,* **104**(6), 2985–3007.

Ebinger, C., 2005. Continental break-up: the East African perspective, *Astron. Geophys.,* **46**(2), 2.16–2.21.

Ebinger, C., Rosendahl, B. & Reynolds, D., 1987. Tectonic model of the Malai rift, Africa, *Tectonophysics,* **141**(1–3), 215–235.

Fenton, C.H. & Bommer, J.J., 2006. The $M_w$7 Machaze, Mozambique, earthquake of 23 February 2006, *Seism. Res. Lett.,* **77**(4), 426–439.

Flores, G., 1973. *The Cretaceous and Tertiary Sedimentary Basins Mozambique and Zululand, in Sedimentary Basins of the African Coasts,* Association of African Geological Survey, Paris.

Fonseca, J.F.B.D. *et al.*, 2014. MOZART: a seismological investigation of the East African Rift in Central Mozambique, *Seism. Res. Lett.,* **85**(1), 108–116.

Fouch, M.J., James, D.E., Vandecar, J.C., Lee, S.V.D. & the Kaapcvaa Seismic Group, 2004. Mantle seismic structure beneath the Kaapvaal and Zimbabwe Cratons, *South Afr. J. Geol.,* **107,** 33–44.

Hartnady, C.J.H., 2006. Seismotectonics of Southern Mozambique, in *21st Colloquium on African Geology (CAG21),* Maputo, 3–5 July 2006, Abstracts Volume, pp. 408–410.

Herrmann, R.B., 2013. Computer programs in seismology: an evolving tool for instruction and research, *Seism. Res. Lett.,* **84**(6), 1081–1088.

Herrmann, R.B. & Ammon, C.J., 2004. *Surface Waves, Receiver Functions and Crustal Structure, Computer Programs in Seismology,* St. Louis University.

James, D.E., Niu, F. & Rokosky, J., 2003. Crustal structure of the Kaapvaal craton and its significance for early crustal evolution, *Lithos,* **71,** 413–429.

Julià, J., Ammon, C.J., Herrmann, R.B. & Correig, A.M., 2000. Joint inversion of receiver function and surface wave dispersion observations, *Geophys. J. Int.,* **143**(1), 99–112.

Kennett, B., Sambridge, M. & Williamson, P., 1988. Subspace methods for large inverse problems with multiple parameter classes, *Geophys. J.,* **94,** 237–247.

Kennett, B.L.N. & Engdah, E.R., 1991. Traveltimes for global earthquake location and phase identification, *Geophys. J. Int.,* **105,** 429–465.

Kgaswane, E.M., Nyblade, A.A., Julià, J., Dirks, P.H.G.M., Durrheim, R.J. & Pasyanos, M.E., 2009. Shear wave velocity structure of the lower crust in southern Africa: evidence for compositional heterogeneity within Archaean and Proterozoic terrains, *J. geophys. Res.,* **114**(12), 1–19.

Kgaswane, E.M., Nyblade, A.A., Durrheim, R.J., Julià, J., Dirks, P.H.G.M. & Webb, S.J., 2012. Shear wave velocity structure of the Bushveld Complex, South Africa, *Tectonophysics,* **554–557,** 83–104.

Kim, S., Nyblade, A.A., Rhie, J., Baag, C.E. & Kang, T.S., 2012. Crustal S-wave velocity structure of the Main Ethiopian Rift from ambient noise tomography, *Geophys. J. Int.,* **191**(2), 865–878.

Kröner, A. & Mainz, U., 2004. Africa/Pan-African orogeny, in *Encyclopedia of Geology,* vol. 1, pp. 1 –12, eds    Selley, R.C., Cocks, L.R. & Plimer, I.R., Elsevier.

Lachelt, S., 2004. *The Geology and Mineral Resources of Mozambique,* República de Mocambique, Ministerio dos Recursos Minerais e Energia, Direccao Nacional de Geologia, Maputo.

Laske, G., Masters, G., Ma, Z. & Pasyanos, M.E., 2013. Update on CRUST1.0 : a 1-degree Global Model of Earth's Crust, *Geophys. Res. Abstr.,* **15,** Abstract EGU2013–2658.

Leinweber, V.T. & Jokat, W., 2011. Is there continental crust underneath the northern Natal Valley and the Mozambique Coastal Plains?, *Geophys. Res. Lett.,* **38**(14), L14303, doi:10.1029/2011GL047659.

Lin, F.-C., Ritzwoller, M.H. & Shapiro, N.M., 2006. Is ambient noise tomography across ocean basins possible?, *Geophys. Res. Lett.,* **33**(14), L14304, doi:10.1029/2006GL026610.

Lobkis, O.I. & Weaver, R.L., 2001. On the emergence of the Green's function in the correlations of a diffuse field, *J. acoust. Soc. Am.,* **110**(6), 3011–3017.

Mcnamara, D.E. & Buland, R.P., 2004. Ambient Noise Levels in the Continental United States, *Bull. seism. Soc. Am.,* **94**(4), 1517–1527.

Nairn, A., Lerche, I. & Iliffe, J., 1991. Geology, basin analysis, and hydrocarbon potential of Mozambique and the Mozambique Channel, *Earth-Sci. Rev.,* **30**(1–2), 81–123.

Nyblade, A., Durrheim, R., Dirks, P., Graham, G., Gibson, R. & Webb, S., 2011. Geoscience initiative develops sustainable science in Africa, *EOS, Trans. Am. geophys. Un.,* **92**(19), 161, doi:10.1029/2011EO190002.

Raucoules, D., Ristori, B., de Michele, M. & Briole, P., 2010. Surface displacement of the Mw 7 Machaze earthquake (Mozambique): complementary use of multiband InSAR and radar amplitude image correlation with elastic modelling, *Remote Sens. Environ.,* **114**(10), 2211–2218.

Rawlinson, N. & Sambridge, M., 2005. The fast marching method: an effective tool for tomographic imaging and tracking multiple phases in complex layered media, *Explor. Geophys.,* **36**(4), 341–350.

Rawlinson, N., Sambridge, M. & Saygin, E., 2008. A dynamic objective function technique for generating multiple solution models in seismic tomography, *Geophys. J. Int.,* **174**(1), 295–308.

Ritzwoller, M.H., Lin, F.-C. & Shen, W., 2011. Ambient noise tomography with a large seismic array, *C. R. Geosci.,* **343**(8–9), 558–570.

Roux, P., Sabra, K.G., Kuperman, W.A. & Roux, A., 2005. Ambient noise cross correlation in free space: theoretical approach, *J. acoust. Soc. Am.,* **117**(1), 79–84.

Russell, D., 1987. Multi-channel processing of dispersed surface waves, *PhD thesis,* University of St. Louis.

Sabra, K.G., 2005. Extracting time-domain Green's function estimates from ambient seismic noise, *Geophys. Res. Lett.,* **32**(3), L03310, doi:10.1029/2004GL021862.

Sabra, K.G., Gerstoft, P., Roux, P., Kuperman, W.A. & Fehler, M.C., 2005. Surface wave tomography from microseisms in Southern California, *Geophys. Res. Lett.,* **32**(14), L14311, doi:10.1029/2005GL023155.

Salman, G. & Abdula, I., 1995. Development of the Mozambique and Ruvuma sedimentary basins, offshore Mozambique, *Sediment. Geol.,* **96**(94), 7–41.

Schlüter, T., 2006. *Geological Atlas of Africa,* Springer.

Shapiro, N.M. & Campillo, M., 2004. Emergence of broadband Rayleigh waves from correlations of the ambient seismic noise, *Geophys. Res. Lett.,* **31**(7), L07614, doi:10.1029/2004GL019491.

Shapiro, N.M., Campillo, M., Stehly, L. & Ritzwoller, M.H., 2005. High-resolution surface-wave tomography from ambient seismic noise, *Science,* **307**(5715), 1615–1618.

Simmons, N.A., Myers, S.C., Johannesson, G. & Matzel, E., 2012. LLNL-G3Dv3: global P wave tomography model for improved regional and teleseismic travel time prediction, *J. geophys. Res.,* **117** (B10), B10302, doi:10.1029/2012JB009525.

Sykes, L.R., 1978. Intraplate seismicity, reactivation of preexisting zones of weakness, alkaline magmatism, and other tectonism postdating continental fragmentation, *Rev. Geophys.,* **16**(4), 621–688.

Wapenaar, K., 2004. Retrieving the elastodynamic Green's function of an arbitrary inhomogeneous medium by cross correlation, *Phys. Rev. Lett.,* **93**(25), doi:10.1103/PhysRevLett.93.254301.

Watkeys, M.K., 2002. Development of the Lebombo rifted volcanic margin of southeast Africa, *Spec. Pap.—Geol. Soc. Am.,* **362,** 27–46.

Watts, A.B., 2001. Gravity anomalies, flexure and crustal structure at the Mozambique rifted margin, *Mar. Pet. Geol.,* **18**, 445–455.

Yang, Y. & Ritzwoller, M.H., 2008. Characteristics of ambient seismic noise as a source for surface wave tomography, *Geochem. Geophys. Geosyst.,* **9**(2), 1–18.

Yang, Z. & Chen, W.-P., 2008. Mozambique earthquake sequence of 2006: high-angle normal faulting in southern Africa, *J. geophys. Res.,* **113**(B12), B12303, doi:10.1029/2007JB005419.

## SUPPORTING INFORMATION

Additional Supporting Information may be found in the online version of this paper:

**Figure S1.** Comparison between different types of time-domain normalization using a daily waveform (01/04/2011) recorded at station A0293. (a) Raw waveform. (b) Processed waveform with instrument response, mean and trend removed. (c) Clipping method applied. (d) Running Absolute Mean Normalization (RAMN) applied.

**Figure S2.** Causal side of a raw cross-correlation of 1 day compared with a raw cross-correlation stack of 6 months for station pair 3522–3434.

**Figure S3.** Example of cross-correlations with SNR lower, equal and larger than 7 (value considered the threshold for cross-correlations acceptance). The cross-correlations presented are filtered for a dominant period of $T \sim 10$ s and self-normalized to 1.

**Figure S4.** Sensitivity Kernels calculated for regions 2 and 3 that correspond to MCP and Kaapvaal craton respectively.

**Figure S5.** 1-D depth inversions profiles for four different selected regions in Mozambique. The red line in all profiles represent the starting model for each particular region and the blue line represents the final model after inversion. CRUST1.0 (Laske *et al.* 2013) was used as reference for the starting models. The misfit errors of the final model are presented in the bottom of each profile. (http://gji.oxfordjournals.org/lookup/suppl/doi:10.1093/gji/ggv538/-/DC1).

Please note: Oxford University Press is not responsible for the content or functionality of any supporting materials supplied by the authors. Any queries (other than missing material) should be directed to the corresponding author for the paper.